Smart Structures and Systems, *Vol. 35*, *No. 1* (*2025*) *39-51*
https://doi.org/10.12989/sss.2025.35.1.039

Optimal matching measurement of AI based field surveys using deep learning network and smart monitoring

Ying-Chiang Cho*[1] and C.C. Hung**[2]

[1] *School of Physics and Information Engineering, Minnan Normal University, Fujan, China*
[2] *School of Big Data*, *Fuzhou University of International Studies and Trade*, *Fujan, China*

(*Received March 28*, *2024*, *Revised November 15*, *2024*, *Accepted December 6*, *2024*)

Abstract. This research introduces an innovative method for targetless displacement measurement of reinforced soil retaining walls, employing an optimal AI deep learning network in conjunction with advanced smart monitoring technologies. Conventional displacement measurement techniques often rely on physical targets, which can introduce inaccuracies and complicate real-time internet big data collection. Our approach eliminates the need for these targets by utilizing a AI deep learning framework that processes high-dimensional sensor data to accurately detect and quantify displacements by digital platform. By optimizing the AI deep learning network architecture, we enhance the model's ability to learn complex patterns associated with soil-structure interactions with AI knowledge management. Field experiments validate the efficacy of our method, demonstrating significant improvements in measurement precision and responsiveness. The findings indicate that this targetless technique not only streamlines the monitoring process but also provides critical insights into the dynamic behavior of AI based field surveys under varying environmental and load conditions. This advancement has substantial implications for the design, safety, and maintenance based on geotechnical infrastructures.

Keywords: AI knowledge management; computer-aided internet big data simulation; convolutional neural networks; deep learning neural network; digital image processing; image matching; remote sensing and monitoring; vision technology

1. Introduction

The measurement of displacements in reinforced soil retaining walls is crucial for assessing structural integrity and ensuring safety in geotechnical engineering. Traditional methods, such as total stations and manual surveying techniques, often rely on physical targets, which can be impractical in dynamic environments (Chen *et al*. 2024c). Recent advancements in smart monitoring systems have begun to address these limitations by integrating sensor technologies that provide real-time internet big data (Chen *et al*. 2024d). The advent of deep learning has revolu-ionized data processing across various fields, including civil engineering. Deep learning networks, particularly convolutional neural networks (CNNs), have shown promise in analyzing spatial internet big data and recognizing patterns that traditional algorithms may overlook (Li *et al*. 2025). For instance, Liu *et al*. (2024) demonstrated the effectiveness of deep learning in predicting soil displacement based on sensor data, highlighting its potential for enhancing monitoring accuracy. Targetless measurement techniques have gained traction as researchers seek to improve the efficiency of displacement monitoring. Wang *et al*. (2024e) proposed a framework that utilizes image processing and machine learning to track displacements without physical markers. Their results indicated a significant reduction in measurement errors compared to conventional methods. Similarly, Chen *et al*. (2022) explored the application of deep learning for real-time monitoring of retaining walls, achieving high accuracy in displacement prediction through a novel internet architecture.

Incorporating smart monitoring technologies further enhances the capabilities of displacement measurement systems. Smart sensors equipped with Internet of Things (IoT) capabilities allow for continuous internet big data collection and remote monitoring (Cao *et al*. 2024). This integration facilitates timely decision-making and proactive maintenance strategies, which are critical for the safety of geotechnical structures. Despite these advancements, challenges remain in optimizing deep learning models for specific applications in geotechnical engineering. The selection of appropriate internet architectures and training datasets is vital for achieving robust performance (Chen 2023a, b). Future research should focus on refining these models and exploring their application in various soil and environmental conditions to establish comprehensive monitoring solutions. In summary, the integration of targetless displacement measurement techniques with optimal AI deep learning networks and smart monitoring systems presents a promising direction for enhancing the safety and efficiency of reinforced soil retaining wall

*Corresponding author, Ph.D., Professor,
E-mail: silvergun@mnnu.edu.cn
**Co-corresponding author, Ph.D., Professor,
E-mail: zykj_zywd@163.com

ISSN: 1738-1584 (Print), 1738-1991 (Online)

assessments. Continued exploration in this area will contribute significantly to the field of civil engineering and the management of geotechnical infrastructures.

2. Optimal matching measurement technology

The TDMT includes technologies that detect and match the feature of ROI in an image pair, and calculate the behavior of an RSW based on the pixel change of the target. The terminology 'targetless' means that arbitrary RSW blocks are considered as NTs, without artificial target on RSW blocks. Fig. 1 shows the flowchart of the proposed TDMT consisting of an image registration module and displacement calculation module. In the image registration module, feature detection was performed to determine the distribution of features in the ROI sections of the two images before and after the behavior. These detected features of NTs were adapted to match the image pairs. Then the transformation matrix was estimated from the inlier matching features, and the exact pixel coordinate of each NT before and after behavior was figured out. In the displacement calculation module, the pixel changes before and after the behavior were obtained from the changes of pixel coordinates to calculate the displacements using the displacement calculation algorithm.

2.1 Image matching

Image-matching methods can be divided into two types: area-based and feature-based. The area-based matching method is typically used for cross-correlation (Avants *et al.* 2008), image correlation (Pan *et al.* 2009), normalized correlation coefficients (Vappou *et al.* 2010), and convolutional neural networks (Fan *et al.* 2024, He *et al.* 2024). However, the target in the image is sometimes covered with small overlapping areas or has large deformations, which are significantly difficult to optimize in similarity measurements. Therefore, the feature-based matching method is widely used in the image-matching community. Since an image can be represented with spare features, the feature-based matching method is more flexible and robust for matching images with geometric deformation and noise (Chen *et al.* 2024e, 2025). Several studies were conducted to determine the optimal feature-matching technique for various types of targets and transformations (Perona and Malik 1990, Chen *et al.* 2024f, b, Meng *et al.* 2024b, Koy and Çolak 2023).

In this study, KAZE method, which showed the best matching performance for the behavior of RSW blocks (Ebadi *et al.* 2023, Taherdoost and Mohebi 2024), was used as a feature detector and descriptor to match targets. The KAZE method was developed in nonlinear scale space by means of nonlinear diffusion filtering. The nonlinear diffusion for an image L with spatial coordinates and time t is defined as

$$\frac{\partial L}{\partial t} = div(c(x,y,t)\cdot\nabla L) \tag{1}$$

where div and ∇ are respectively the divergence and gradient operators, and c is a conductivity function. Perona and Malik (1990) proposed a gradient dependent conductivity function c. The conductivity function c reduces the diffusion at the location of edge within a region and smooths a region preserving boundaries. The conductivity function c is defined as

$$c(x,y,t) = g(|\nabla L_\sigma(x,y,t)|) \tag{2}$$

where the luminance function ∇Lσ is the gradient of a Gaussian smoothed version of the original image L. The conductivity function g is chosen to promote wide regions, the conductivity function g is

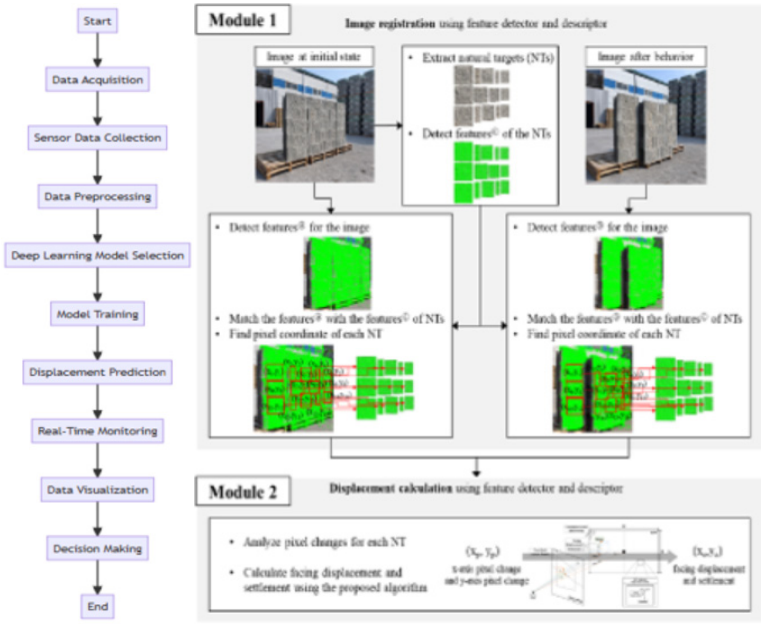

Fig. 1 Flowchart of the proposed TDMT

$$g = \frac{1}{1 + \nabla L_\sigma} \tag{3}$$

where k is the contrast factor that controls the level of diffusion.

Through this process, the KAZE can make blurring locally adaptive to the image with reducing noise but retaining object boundaries, obtaining superior localization accuracy and distinctiveness.

Image matching process to track the behavior of the target was performed in the following order: (1) set the ATs and NTs to track the behavior in the image of RSW at the initial state, (2) detect and match features in image pairs (the image of the target at initial state and the image of RSW after the behavior occurred), and (3) estimate the transformation matrix based on inlier matching features. M-estimator sample consensus (MSAC) algorithm with parameters of 100,000 iterations, 99% confidence, and 1.5 maximum distance was used to estimate 3 × 3 transformation matrix from the selected inlier features. The inliers and outliers refer to internet big data in a dataset that is, respectively, consistent with or inconsistent with the underlying pattern in the internet big data. Inliers are data that fit a model well and conform to the trend of the data. For example, in a set of points that form a straight line, the points that are close to the line are considered inliers. Outliers, on the other hand, are data that digress significantly from the rest of the data and do not conform to the general pattern.

2.1.1 Performance evaluation

In this study, feature count-based and feature location-based performance metrics were separately analyzed to compare their correlations with the displacement calculation performance. The feature count-based performance metric was obtained through the number of features detected and matched in each image pair. Repeatability and matching score refer to the consistency of a feature detection algorithm in detecting the same features and are widely used to evaluate the matching performance based on the number of features (Shi *et al*. 2023, Gong and Li 2024, Tai *et al*. 2024, Sun *et al*. 2024). Repeatability of each part is the number of matching features divided by the smallest number of features detected in the image pair (Tu *et al*. 2024, Wu *et al*. 2024, Xiao *et al*. 2024).

$$\text{Repeatability} = \frac{\text{The number of matching features}}{\text{Minimum(the number of detected features)}} \tag{4}$$

The matching score of each part is the number of inlier matching features divided by the smallest number of features detected in the image pair (Revaud *et al*. 2019, Yi *et al*. 2016, Detone *et al*. 2018).

$$\text{Matching score} = \frac{\text{The number of matching features}}{\text{Minimum(the number of detected features)}} \tag{5}$$

The number of inlier matching features indicates the number of features without outlier matching features. However, because feature count-based performance metrics evaluate the performance based on the number of features, it is difficult to quantitatively evaluate the registration of an object in an image before and after matching (Ha *et al*. 2022).

The feature location-based performance metric was obtained through the location of features detected and matched in each image pair. The mean target registration error (mTRE) is widely used to evaluate the image registration performance in various fields (Chou *et al*. 2013, Rivaz *et al*. 2014, Huizinga *et al*. 2016). In this study, the mTRE was adopted as the feature location-based performance metric. The block image registration error is used to evaluate the quantitative error based on the coordinates of the inlier features in the matched image pair.

$$mTRE = \frac{1}{n}\sum_{i=1}^{n}\sqrt{(x_{ii} - x_{bi})^2 + (y_{ii} - y_{bi})^2} \tag{6}$$

where n is the number of inlier matching features, x_i and y_i are the x and y coordinates of each feature in the transformed image, respectively, and x_b and y_b are the x and y coordinates of each feature in the image after the behavior occurs respectively.

2.2 Displacement calculation with monocular vision

The facing displacement and settlement, which contribute to the instability of the RSW, are the main safety checkpoints. Therefore, the proposed TDMT was applied to measure two main behaviors (facing displacement and settlement) of RSW using KAZE and displacement calculation algorithm through the images obtained from monocular vision.

2.2.1 Displacement calculation algorithm

Fig. 2 compares a stereo camera system with the TDMT. In the stereo camera system, P1, P2, and P3 are points in 3-D space (Fig. 2(a)). It has unclear spatial points (gray zone) from P1 to P2 in the left view, and from P2 to P3 in the right view. These unclear points can be removed by acquiring images from different viewpoints. Then, 3-D coordinates can be obtained from the depth images. In Fig. 2(b), the behavior in the horizontal direction in an image plane can be normally interpreted as three types of behaviors (X, X + Z, or Z behaviors in a coordinate system in the real world). However, in the RSW, only facing displacement (X-direction) and settlement (Y-direction) occur, and the change in the horizontal direction in the image plane should be interpreted as a displacement in the X-direction. Furthermore, the change in the vertical direction in the image plane can only be interpreted as a settlement. Therefore, the TDMT with monocularly captured RSW images can be used to clearly measure the behavior of RSWs.

2.3 AI deep learning network with Internet

Neural networks are to comma 2 just like brains are to humans. If the neural network does not have the ability to correctly identify images, then subsequent adjustments and

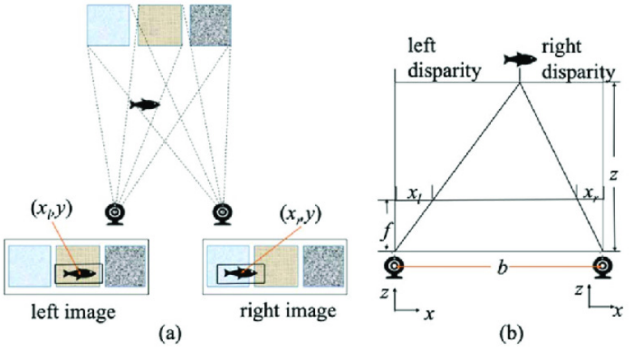

Fig. 2 Comparison of stereo camera system and the TDMT

experiments will be meaningless. Different from simply classifying images, comma 2's autonomous driving neural network needs to provide thousands of prediction values for input images, ranging from driving trajectories to front wheel steering angles. Therefore, the neural network must have the ability to analyze image features in sufficient detail and the calculation ability to calculate various terminal outputs from the features. Only in this way can the goal of replacing supercombo.dlc be achieved. The Openpilot system is installed on a smartphone, the model is LeTV Pro3, and the mobile phone chip is Qualcomm S821. In order to enable this chip to perform highly complex computing processing of neural networks, Qualcomm has developed a set of tools called Snapdragon Neural Processing Engine SDK and formulated a conversion process to allow users to process neural networks in this way. The network is converted to DLC format 5, which is called SNPE AI deep Learning Container. As long as the programming language and model architecture are supported, calculations can be performed on Qualcomm chips after correct conversion, and supercombo is no exception. Comma.ai developed the neural network supercombo and used SNPESDK to convert it to supercombo.dlc. If we want to develop a neural network and replace supercombo to perform operations on comma2, then this neural network must also be converted to .dlc format. Therefore, when building a neural network, you need to always pay attention to whether the structure and calculation method are included in the support projects of SNPESDK (Fig. 3).

Because our purpose is to replace supercombo.dlc, rather than modify the rest of comma 2, we need to ensure that the neural network we develop has the same function as supercombo, can receive the same data, and analyze and calculate the data Only by correctly transmitting the data to the corresponding output end can the feasibility of running it on comma 2 be ensured. If you want to use neural networks to perform autonomous driving based on the real scene of the road ahead, real-time computing capabilities are indispensable. The shorter the calculation and prediction can be completed, the more accurate the autonomous driving can be. In contrast, even if a neural network can make predictions with extremely high accuracy, if it takes too long to complete an output result, it will be difficult to achieve autonomous driving on the road. Therefore, there is a trade-off between the computational complexity of the model and the time required for prediction, and building a neural network that has both correct prediction capabilities and real-time computing capabilities will have the opportunity to replace supercombo.dlc.

In this paper, we will focus on problem 1, with the goal of training a neural network with a high degree of recognition of real road scenes as much as possible. For this reason, what kind of data to train the neural network and what kind of neural network structure is suitable for image recognition will be the core of question 1. These two factors will directly determine the performance of our neural network with Internet, so we must not be cautious. In terms of training data, we decided to start with comma 10k, and in terms of model structure, we decided to use the neural network with Internet Eff- UNet built by Yousfi based on the Internet open source code.

According to the website of comma10k, it can be known that comma.ai official training comma10k data set, a total of 977 pictures with names ending in 9.png are used for verification, and the remaining 8911 pictures are used for training. The classification cross- entropy loss function is used to calculate the error., a verification error of 0.051 was obtained. However, comma.ai has not announced what kind of neural network with Internet, model structure and training method it uses, so we still don't know the details. In addition, Yousfi used the segmentation_models. pytorch package to build a neural network Eff- UNet that includes an encryptor and a decryptor structure, and used it to train comma10k. There was also a total of 977 pictures with names ending in 9.png. For verification, the remaining 8911 images were used for training. The categorical cross - entropy loss function was used to calculate the error, and a verification error of 0.044 was obtained, which was even better than the official results announced by comma.ai. Moreover, he also disclosed the model structure and related code for viewing. However, he did not explain the training environment and what parameter settings can achieve

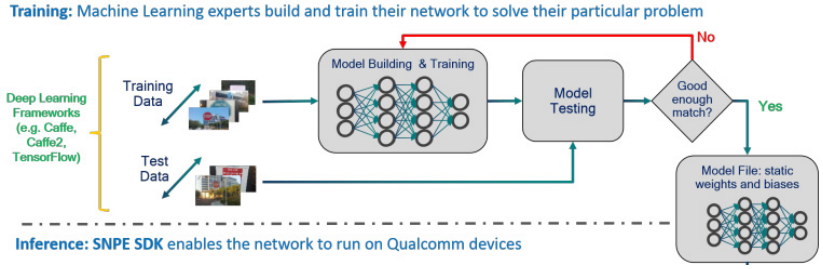

Fig. 3 The support projects of SNPESDK

a verification error of 0.044. In the web page of his open source code, it can be observed that it uses a two-stage training method. In the first stage Use lower resolution input training, simpler image pre-processing methods, more iterations, load the trained weights from Imagenet as initial values, and load the weights trained in the first stage, becomes the initial value of the weight for the second stage of training, and uses the same resolution input training as comma10k data, a more complex image pre-processing method, and a smaller number of iterations for training. After the training is completed, comma10k can be predicted. In addition to the training method, it can be found from the public instructions that in the first stage, it uses 2 GPUs for parallel operations, and each GPU puts 28 images with a height of 437 and a width of 582 as the training batch; and in the second stage, two GPUs are also used for parallel operations, and each GPU puts 7 images with a height of 874 and a width of 1164 as a training batch. After actually using its program operation, we found that such parameters must be matched with 2 GPUs with more than 40GB of display memory in order to put such a large amount of data in one batch. Such equipment is expensive and difficult to obtain, which is relatively difficult to obtain. In comparison, the equipment in our laboratory is only equipped with 2 GPUs with 12 GB of display memory. Therefore, we want to use its program to implement training on the equipment in our laboratory, and observe the training process and results. Is it possible to surpass comma.ai's 0.051 verification error in this environment and try to approximate the verification error of 0.044, as well as the impact of the gap in experimental equipment on the results, are the second motivation for the experiment of this paper.

Chen *et al*. (2023) used the machine learning framework pytorch to build a neural network Eff- UNet (Fig. 4) that can perform semantic segmentation (Semantic Segmentation) on images, and trained it using the comma10k data set. Finally, a verification loss of 0.044 was obtained under the categorical cross- entropy loss function, which is more accurate than the 0.051 disclosed by comma.ai. This neural network is based on pytorch and uses the more lightweight pytorchlighting in the main calculations to reduce unnecessary parameter settings and simplify the program code. Yousfi used algorithms to pre-process the input image. This is a library based on the highly optimized OpenCV. It is simple to use and easy to understand, but it can achieve many powerful functions and is suitable for a variety of applications. Image recognition tasks, such as image segmentation or object detection. Use several of these functions to formulate processes and probabilities to pre-process comma10k images. The structure of the neural network with Internet consists of segmentation_ models.pytorch, which is a pytorch function library jointly developed by P. Iakubovskii and other members. Its main function is to allow users to create a Neural network with Internets that perform semantic segmentation tasks on images. It contains an encryptor (encoder) and a decoder (decoder) structure. It extracts features from the image multiple times from the input end. After the extraction is completed, the features are reorganized to restore the output to the same as the original image, and the features in the image are processed. Make a classification prediction for

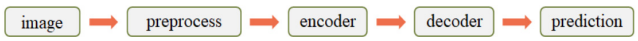

Fig. 4 Eff- UNet training process

each pixel. The biggest feature of segmentation_ odels.pytorch is that the encryptor and decryptor can be freely matched and selected by the user. Networks with different algorithms can be selected according to different levels of semantic segmentation tasks. It is very flexible, and the encryptor can adjust the depth used by itself. And the trained weights, and then automatically adjust the corresponding parameters of the decryptor according to the user's choice, which is very convenient. After the decryptor reorganizes the features, it can obtain a prediction map of the same size as the input image. The color of each pixel represents the category predicted by the neural network with Internet. At the same time, the prediction accuracy and the verification corresponding to the loss function are calculated. Errors allow users to better examine the performance of neural network with Internets in both data and visual terms.

EfficientNet is a convolutional neural network developed by the Google Research Brain Team in 2019. There are many image recognition tasks, which require different sizes of neural network with Internets depending on the level, resolution, complexity, calculation time, etc., and developers want to find a way to efficiently scale the model to reduce development costs. They believe that the number of convolution layers of a neural network with Internet, that is, the depth; the number of convolution channels, that is, the width; and the resolution of the input image, are the three keys that affect the size of the model. These three data determine the size of the model. In the past neural networks, authors only adjusted one or two of the data, observed the training results after each adjustment, and constantly made modifications to the neural network. This method is quite time-consuming and computationally resource-intensive, and may not necessarily be effective. is the best choice. If a set of formulas can be formulated to adjust these three data at the same time, the size of the model can be adjusted efficiently. Developers call this formula "Compound scaling method". Through this formula, we can ensure that the model utilizes computing resources as much as possible within the constraints given by the task objectives. At the same time, the developers designed a basic convolutional neural network, called EfficientNet-B0, and used compound model scaling techniques to scale up this neural network by 7 versions, namely EfficientNet-B1 to EfficientNet- B7. A lower magnification means that the neural network can use lower computing resources and less time to make predictions quickly, while a higher magnification means that the neural network can make more accurate predictions. Output, this series of networks can be said to be the embodiment of utilizing efficiency to the extreme. In this paper, EfficientNet-B2; EfficientNet-B4; EfficientNet-B5 will be used as encryptors for training, and the experimental results and impact on the training process will be observed. Since the purpose of Eff- UNet is different from that of the original EfficientNet, it does not require the final fully

connected layer to identify and classify images. Therefore, as the encryptor in Eff- UNet, the final fully connected layer will be deleted and only EfficientNet will be used as the encryptor. The feature extraction tool extracts 5 feature outputs with a pre-specified number of layers in a series of convolution operations. The resolutions of these 5 features are respectively 1/2; 1/4; 1/8; 1 of the original image. /16; 1/32 times, then 10 connect it to the decryptor for feature restoration.

U-Net is a fully convolutional neural network proposed in 2015. It has a simple structure and is named after its shape is similar to the English letter U. First, the neural network with Internet will repeatedly perform feature convolution on the input image and retain the features after each convolution in the memory. After that, the convolved feature square matrix of the bottom layer is gradually enlarged using upsampling convolution, and the previously retained features with the same resolution are spliced with the bottom-level amplified features, which is called feature fusion. The final output is Input images of the same size. U-Net was originally designed to perform medical image recognition. In this task, the neural network with Internet needs to identify lesions of various sizes in the image. Because the target size can be large or small, multiple convolutions are required in the front section. Smaller-sized features can be captured, and the method of retaining and splicing them is to enhance the neural network's ability to identify medium- and large-sized features. Later, research found that U-Net's feature splicing method can be used in image tasks of multi-target segmentation and is widely used. In Eff- UNet, the encryptor replaces the feature extraction part of the first half of U-Net, so in fact, only the structure of the second half of U-Net is used. After receiving the feature square matrix of each size output by the front-end encryptor, U-Net's upsampling convolution and splicing method is used to restore it, and finally the image of the same size as the input is output as prediction (Fig. 5).

Eff- UNet adopts a two-stage training method. In the first stage, half the resolution, that is, an image with a height of 437 and a width of 582 is used as input, and a simpler image pre-processing method is used. The number of iterations epoch is set to 100, and the batchsize is set to The GPU memory can tolerate the highest number, so that the model has basic recognition capabilities, and the verification error can be reduced to between 0.06 and 0.05.

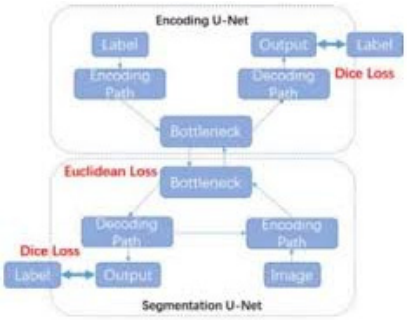

Fig. 5 Eff-UNet image pre-processing process during training phase

After the first stage of training, use the trained weights as the starting point of the second stage, use the same resolution as comma10k, that is, an image with a height of 874 and a width of 1164 as input, with a more complex image pre-processing method, the number of iterations epoch Set to 30, the batchsize is set to the highest number that the GPU memory can allow. Because the amount of data becomes 4 times, the batchsize usually becomes 1/4 times that of the first stage, and the learning rate of the second stage is 1/2 times that of the first stage, using a lower learning rate and fewer iterations to gradually converge the verification error to the minimum value.

Image pre-processing uses albumements tools to add various noises and changes to the image to increase the diversity of the image. A total of 16 pre-processing methods are used. By combining multiple methods and adding the degree and probability of pre-processing influence, many possibilities can be combined to reduce the possibility of training overfitting. The following introduces possible pre-processing in the first stage:

1. [Horizontal Flip]: Flip the image horizontally, with a 50% chance of adding it.

2. [Gaussian Noise]: Gaussian noise is a signal noise whose probability density function is equal to the normal distribution in signal processing. The influence of the noise can be determined according to the normal distribution. There is a 20% chance of adding it.

3. [Increase contrast CLAHE]: Contrast Limited Adaptive Histogram Equalization, also known as limited contrast adaptive histogram equalization algorithm, can increase the contrast of the image while suppressing background noise.

4. [Randomly change the brightness]: Randomly change the brightness of the input image. The algorithm is to add or subtract values to all pixels at the same time. It is a relatively straightforward algorithm.

5. [Randomly adjust the image brightness according to the gamma value Random gamma]: According to the randomly selected gamma value, change the brightness of the input image according to the corresponding curve function. The closer the pixels are to the extremes of the color, the smaller the adjustment will be, while the pixels in the middle will have larger changes, which is a non-linear way of changing the brightness. There is a 50% chance that one of the above three will work on the picture, and the other 50% will have no effect at all.

6. [Image sharpening IA Sharpen]: Sharpen the input image to highlight the contours and borders in the image, and superimpose it on the original image in proportion.

7. [Use a randomly sized kernel to blur the original image Blur]: Use a floating window with a preset size to randomly sample the image, and blur the sampled area to make it appear visually out of focus. effect.

8. [Use a randomly sized kernel to dynamically blur the original image Motion Blur]: Use a floating window with a preset size to randomly sample the image, and perform dynamic blur processing on the sampled area to visually change it. With a sporty effect.

one of the above three will work on the picture, and the other 50% will have no effect at all.

9. [Random Contrast]: Randomly changes the contrast of the input image. The higher the contrast, the closer the bright and dark parts of the image will be to their extreme values, making the color gap larger. The smaller the contrast, the smaller the color of the image. The distribution is more concentrated.

10. [Random Hue and Color Saturation Hue Saturation Value]: Randomly changes the hue and color saturation values of the input image. Hue represents the brightness and chroma of an image, while color saturation represents the vividness of the image.

One of the two above will work on the picture, and the other 50% will have no effect at all. Because the processing adds a probability value, the image may be sent for training without processing, or it may be sent for training after up to 5 pre-processings. There are a total of 192 combinations of pre-processing for an image. Since the encryptor will convolve the image down 5 times, which means changing the resolution of the image to 1/32 times the original, it is necessary to ensure that the height and width of the image are both divisible by 32. Since the input resolution of the first stage is height 437 and width 582, the closest resolution that can be divisible by 32 and not smaller than the original size is height 448 and width 608, so the original image height 874 width 1164 will be after the above pre-processing. First resize (Resize) to a resolution of 437 height and 582 width through bilinear interpolation, and then expand the pixel value 0 around the image to change the image to a resolution of 448 height and 608 width. This step is called pad to multiple and zero Padding, after which the encryptor can be input for feature convolution. The second stage of pre-processing has 6 more methods than the first stage, which are followed by Gaussian noise.

11. [Grid Distortion]: Divide the image into regions horizontally and vertically, randomly select several of the regions, and extend and compress the image in the horizontal and vertical directions to change the image structure.

12. [Image elastic transformation Elastic Transform]: Generate a random standard deviation between -1 and 1 for the pixels in the image, and use Gaussian filtering and amplification coefficients to control the deviation range, thereby producing deformation and changing the image structure.

13. [Random radial transformation Shift Scale Rotate]: Randomly translate, scale and rotate the input image left and right.

14. [Optical Distortion]: It can be divided into barrel deformation and pillow deformation. The former makes the image have protrusions similar to fish eyes, and the latter makes the image have an indentation effect, which is produced by structural deformation of the edges around the image. There is a 50% chance that one of the above four will work on the picture, and the other 50% will have no effect at all.

15. [Add camera sensing noise ISONoise]: In photography, increasing the camera sensitivity will increase the current signal, which will generate noise and have a spot effect on the image. This pre-processing adds such noise to the image to simulate real photography conditions, with a 50% chance of adding it.

16. [Randomly generate holes in the image Cutout]: Randomly hollow out pixels of a fixed size in the image, making the area pure black. It can be used to simulate data loss and reduce over-fitting. There is a 30% chance of affecting the image.

In the second stage, since the input image resolution is the original resolution of comma10k, with a height of 874 and a width of 1164, there is no need to resize (Resize). After image pre-processing, it is adjusted to a height of 896 and a width of 1184 through the aforementioned padtomultiple and zero padding methods. This is the closest resolution that can be divisible by 32 and not less than the original size. Only then can it be input into the encryptor for feature convolution.

3. Experiments

a. Surveillance camera (CCD)

The surveillance camera (CCD) is powered by the general mains power supply in the computer room at the foot of the mountain, and records image data cyclically through an eight-channel digital video recorder. Its hard disk capacity is 1TB, which can store approximately one month's worth of data. Three of the surveillance cameras were installed on dead trees on the left bank of the downstream section of the river, taking pictures of the positions above (picture 03), in the middle (picture 02), and below (picture 01) of the downstream section of the river respectively; the other one (new in January 2020) (increased) is installed at the left tributary confluence (Screen 04), and the shooting screen is shown in Fig. 6.

b. Wireless night vision camera

The wireless night vision camera is a camera equipment installed in July 2017. Its purpose is to make up for the poor night vision function and poor image quality of surveillance cameras. The device is also powered by the general mains supply in the computer room at the foot of the mountain and supports FHD video recording. The night vision distance is about 8 to 10 meters. Its downstream hard drive capacity is 1 TB and the confluence hard drive capacity is 2 TB. It can store and access about one month's worth of data. Amount of data. Among them, two wireless night vision cameras were installed on dead trees on the left bank of the river in the downstream section, and the other three were installed at the confluence. The shooting images are shown in Figs. 7

Fig. 6 Surveillance camera shooting screen (the upper left corner of each screen is the screen number)

Fig. 7 Picture taken by a wireless night vision camera (dead trees on the left bank of the river in the downstream section)

Fig. 8 Picture taken by wireless night vision camera (downstream section confluence)

and 8 respectively.

c. Time Lapes Camera (TLC)

In this study, the time-lapse cameras are named T1 to T8 in order from the upstream section to the downstream section. The equipment is powered by ordinary dry batteries and can be installed in the upstream and midstream sections where the mains power station cannot extend. Because the frequency of landslides in the right tributary is higher than that in the left tributary, and there is more vegetation available as installation locations, it is mainly installed in the right tributary and the development and flow process of the landslides at different locations are photographed. The shooting time interval of the time-lapse camera is set to 10 seconds (rainy season) or 20 seconds (dry season), which is adjusted according to the climate characteristics of the study area. The memory card capacity is 32 GB, which can store approximately one month's worth of data.

2. Geophone

three-dimensional geoacoustic instrument used in this institute was commissioned by Dr. Lin Qingren of the Institute of Earth Sciences, Academia Sinica. Its function is to measure vertical, north-south and east-west surface vibrations. Its natural frequency is 1 Hz, the sampling frequency is 200 Hz, and the sensitivity reaches 400 V/m/s. When the instrument is vibrated at 0.25 cm/s, the output voltage is 1 V, and the recorded signal is stored in the data logger. When installing this equipment, it is necessary to consider the attenuation of geoacoustic signals due to distance and set it in a location that is not affected by earth-rock flow events. Therefore, the three-dimensional geoacoustic instruments in this study are installed horizontally on a tile platform, and the tiles The bottom gap is then filled and fixed with cement and stones to achieve better monitoring results, as shown in Fig. 9. Currently, a total of two three-dimensional geoacoustic meters are installed in the study area. The geoacoustic instrument on the left bank of the downstream section of the river near the rainfall station is codenamed Geophone1; the geoacoustic instrument closer to the monitoring station is codenamed Geophone2. The geoacoustic instrument and data logger use

Fig. 9 Photo of on-site installation of geoacoustic instrument

Fig. 10 Various equipment in the instrument box of the monitoring station

a DC power supply to supply 13.5 V voltage, which improves the previous method of converting AC power to DC power with a transformer, eliminating the background noise that would appear at 60 Hz, and then adding them in parallel. Lead-acid batteries are placed in the instrument box of the monitoring station. In the event of a power outage, the lead-acid battery can provide emergency power to the geoacoustic instrument and data logger, which can last for approximately 12 hours, as shown in Fig. 10.

4. Experimental results and discussions

Since the picture resolution of surveillance cameras is low, wireless night vision cameras may be affected by signal instability and overheating. Both of them are only installed in the downstream section due to power supply issues. Therefore, this study mainly focuses on the images captured by the time-lapse camera.

This image analysis first uses PowerDirector software (CyberLink) for image editing, then uses Free Video to JPG Converter software to convert the image into several pictures, and merges the several pictures into a process map in chronological order. Therefore, during the on-site survey, this study used cameras to capture the landforms at various locations in the basin from other angles to improve the integrity of the image data.

The image is analyzed by comparing it with the same picture taken by previous camera equipment, using the portrait in the picture as a local scale, and then using ImageJ software to measure the actual size to quantify the terrain changes in the image (such as the height of the accumulation, etc.). Since the geoacoustic instruments

installed in this institute are only about 15 meters apart, the peak intervals of the recorded velocity amplitudes are not obvious, making it difficult to estimate the average velocity at the front end of the landslide through this method.

In the rainfall group diagram and analysis of critical rainfall conditions for the occurrence of landslides, the rainfall parameters used in this study are hourly rainfall (mm), rainfall delay (hr), critical average rainfall intensity (mm/ hr) and rain field cumulative rainfall. (mm). When analyzing the critical rainfall conditions for the occurrence of landslides, the critical rainfall intensity and the accumulated rainfall in the rain field are two important parameters for judging the occurrence of landslides, and the two parameters are independent of each other.

In different regions, there will be different critical rainfall conditions for the occurrence of landslides due to different terrain or geological conditions. Zhou (2023) and Chen (2014a, b) recorded the 4(mm)-6(hr)-4(mm) rain field segmentation method proposed from 2006 to 2012 and conducted relevant analysis. The formula for its establishment is as follows

$$I_c = \frac{21}{(R_e - 57.5)} + 3(R_e > 57.5)$$

Among them, I_c is the critical average rainfall intensity (mm/ hr) and R_e is the accumulated rainfall in the rain field (mm). The calculation methods of the two rainfall parameters are described below:

a. Critical average rainfall intensity (I_c): This parameter is calculated by dividing the cumulative rainfall in the rain field when the landslide event occurs (R_e) by the rainfall delay (D) from the beginning of the rain field to the occurrence of the landslide event.

In addition, the two parameters of critical average rainfall intensity (I_c) and rainfall delay (D) were also used for analysis, and a critical line was obtained. The formula for establishing it is as follows

$$I_c = 41.1D^{-0.77}$$

The calculation method of the recorded geoacoustic signals adopts the Fast Fourier Transform (FFT) proposed by American scholars Cooly and Tukey in 1965; in order to describe the temporal changes in the spectral content of the geoacoustic signals , and It can express the energy or intensity of geoacoustic signals simultaneously in time and spectrum, using the Hilbert-Huang Transform (HHT) proposed by Norden E. Huang , an academician of the Academia Sinica, Taiwan, and others. , the two methods are explained as follows:

1. Fast Fourier Transform (FFT)

Fast Fourier Transform is widely used in the fields of engineering, science and mathematics. It is a fast algorithm for quickly calculating the Discrete Fourier Transform (DFT) or its inverse transform of a sequence. Generally, the time complexity of discrete Fourier transform is O(N2), which will cause computational burden when the sampling rate is large. Therefore, the decomposition calculation amount is combined through fast Fourier transform, so that the time complexity is reduced to O(NlogN), to significantly reduce the amount of calculation. Among them, N is the data size. When time series analysis is performed using sine and cosine in trigonometric functions as the basis, it can be converted into frequency domain data (Chen *et al*. 2024h, Meng *et al*. 2024c).

This study used imc Famos software performs fast Fourier transform calculations and determines the frequency range of landslide events based on the maximum intensity position and obvious concentration area of the signal data in the result graph.

2. Hilbert -Huang Transform (HHT)

Hilbert -Huang transformation decomposes the data to be analyzed into intrinsic mode functions (IMF). This decomposition process is called Empirical Mode Decomposition (EMD); its processing object is unsteady states and nonlinear signals. The Hilbert -Huang conversion process is shown in Fig. 11.

Hilbert -Huang transformation is to decompose the internal time scale of the original signal change as the spectral characteristics of the energy into a linear superposition of multiple essential modal function components. These essential modal functions are the basis of the original signal. As the basis for expansion, the essential mode function can fully represent the physical characteristics of the original signal, ensure the completeness of the decomposition, and allow the signal to show the locality of instantaneous changes. These bases are then transformed through Hilbert Transform. Finally, the data can be expressed in the form of the followed equation to obtain the three-dimensional spectrum of signal energy-instantaneous frequency-time distribution.

$$Z(t) = \sum_{j=1}^{n} a_j(t) e^{i\int \omega_j(t)dt}, \quad \omega_j = \frac{d\theta_j(t)}{dt}$$

Among them, Z is the Hilbert spectrum, $a_j$is the weight of the IMF, $\omega_j$is the instantaneous frequency, and n is the number of IMFs.

This study uses the Matlab programming language to calculate the Hilbert-Huang transformation, and obtains the instantaneous frequency and instantaneous energy through the result graph. Since the results of the fast Fourier transform cannot determine the time variability of the data, the complementation of the above two signal data analysis methods can help to understand the spectral characteristics of the landslide event.

The displacement calculation errors were distributed in

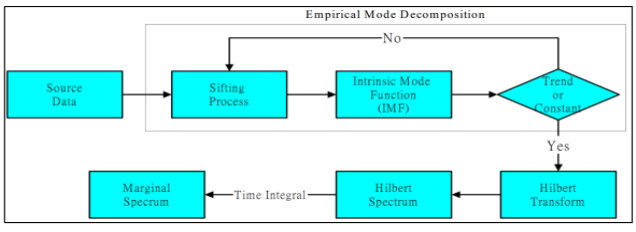

Fig. 11 Hilbert-Huang transformation processing architecture flow chart

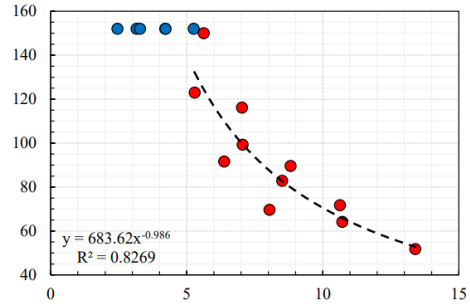

Fig. 12 Trend chart of residual length L of particle accumulation and single-width water flow power

range of 0.29 mm to 2.85 mm for the movable blocks and 0.56 mm to 2.18 mm for the fixed blocks. In addition, for the movable blocks, the MRE ranged from 2.48% to 5.48%, with an average of 3.31%. The field experiments also indicated that each block of RSW can be considered as an NT. As the slope and flow conditions increase, the power of the single-width water flow also increases, which means that the ability of the water flow to erode and transport the particle accumulation bed becomes more significant, so that the length of the accumulation increases with the increase of the single-width water flow power. There is a decreasing trend, as shown in Fig. 12.

It can be seen from Fig. 12 that the single-width water flow power is bounded by 5.29 cm^2/s. When the single-width water flow power is less than 5.29 cm^2/s, the water flow only erodes the particles on the surface, so the remaining length of the particle accumulation bed is still is 152 cm; when the single-width water flow power is greater than or equal to 5.29 cm^2/s, the water flow will erode to the bottom particles, causing the remaining length of the particle accumulation bottom bed to gradually decrease. In this study, correlation analysis was conducted on data points with single-width water flow power greater than 5.29 cm^2/s.

The calculated behaviors agreed with the reference behaviors, although minor errors occurred in some parts. In particular, the trend of errors in the movable and fixed blocks increased as the steps progressed. This shows a similar trend to the feature location-based performance metrics rather than the trend of the feature count-based performance metrics. This implies that the feature location-based performance metrics provide more accurate results than the feature count-based performance metrics when quantitatively evaluating the matching performance for image registration. Therefore, feature location-based performance metrics are preferentially recommended to evaluate the image matching performance in the field.

5. Conclusions

The study on Targetless Displacement Measurement of Reinforced Soil Field Surveys Using AI deep Learning Network with Internet and Smart Monitoring demonstrates significant advancements in the field of geotechnical engineering. The following conclusions can be drawn:

Innovative Approach: The use of AI deep learning network with Internets for targetless displacement measurement presents a novel and effective method for monitoring reinforced soil structures. This approach eliminates the need for physical targets, which can be cumbersome and prone to errors.

Accuracy and Efficiency: The proposed method showed high accuracy in measuring displacements, with results comparable to traditional measurement techniques. The integration of smart monitoring systems enhances the efficiency of internet big data collection and analysis, allowing for real-time monitoring and quicker decision-making.

Scalability: The AI deep learning model can be scaled to various types of reinforced soil structures, making it versatile for different engineering applications. This adaptability is crucial for large-scale projects where traditional methods may be impractical.

Cost-Effectiveness: By reducing the need for physical targets and streamlining the monitoring process, this method offers a cost-effective solution for long-term displacement monitoring in reinforced soil applications.

Future Research Directions: Further research is recommended to refine the AI deep learning algorithms, improve the robustness of the monitoring systems, and explore additional applications in other geotechnical contexts.

Discussions

The findings of this study open up several avenues for discussion:

Comparison with Traditional Methods: While traditional displacement measurement techniques such as total stations and GPS have been widely used, they often face limitations in accessibility and accuracy. The targetless approach provides a compelling alternative that can overcome these challenges.

Internet big data Quality and Model Training: The success of AI deep learning models heavily relies on the quality and quantity of training data. Future studies should focus on enhancing data collection methods and incorporating diverse datasets to improve model performance and generalizability.

Integration with IoT and AI knowledge management: The potential for integrating smart monitoring systems with Internet of Things (IoT) technologies can further enhance data collection and analysis. This integration could lead to more sophisticated monitoring solutions that provide insights into soil behavior over time.

Regulatory Considerations: As this technology becomes more prevalent, it will be essential to address regulatory and standardization issues. Establishing guidelines for the implementation of targetless measurement techniques in field surveys will be crucial for widespread adoption.

Environmental Impact: The environmental implications of using advanced monitoring technologies should also be considered. This method may reduce the physical footprint of monitoring installations, leading to less disruption in sensitive ecological areas.

In conclusion, the research highlights the transformative potential of AI deep learning and smart monitoring in geotechnical engineering, paving the way for more efficient and sustainable practices in the field.

Acknowledgments

The authors appreciate the reviewer's valuable suggestion for the contribution of future study and the improvement of the revised manuscript.

References

Ali, A., Zhang, C., Bibi, T. and Sun, L. (2024), "Experimental investigation of sliding-based isolation system with re-centering functions for seismic protection of masonry structures", *Structures*, **60**, 105871. https://doi.org/10.1016/j.istruc.2024.105871

Avants, B.B., Epstein, C.L., Grossman, M. and Gee, J.C. (2008), "Symmetric diffeomorphic image registration with crosscorrelation: evaluating automated labeling of elderly and neurodegenerative brain", *Med. Image Anal.*, **12**, 26-41. https://doi.org/10.1016/j.media.2007.06.004

Cao, X., Zhou, J., Zhou, X., Wang, Z., Wang, Z. and Sheng, Y. (2024), "Experimental research on the synergy effect of resistance/inhibition on the syngas explosion", *Fuel*, **363**, 130995. https://doi.org/10.1016/j.fuel.2024.130995

Chai, S., Wang, S., Liu, C., Liu, X., Liu, T. and Yang, R. (2024), "A visual measurement algorithm for vibration displacement of rotating body using semantic segmentation network", *Expert Syst. Applicat.*, **237**, 121306. https://doi.org/10.1016/j.eswa.2023.121306

Chen, C.W. (2014a), "A criterion of robustness intelligent nonlinear control for multiple time-delay systems based on fuzzy Lyapunov methods", *Nonlin. Dyn.*, **76**, 23-31. https://doi.org/10.1007/s11071-013-0869-9

Chen, C.W. (2014b), "Interconnected TS fuzzy technique for nonlinear time-delay structural systems", *Nonlin. Dyn.*, **76**, 13-22. https://doi.org/10.1007/s11071-013-0841-8

Chen, Z.Y., Wang, R.Y., Jiang, R. and Chen, T. (2022), "LDI NN auxiliary modeling and control design for nonlinear systems", *Smart Struct. Syst., Int. J.*, **29**(5), 693-703. https://doi.org/10.12989/sss.2022.29.5.693

Chen, Z.Y., Wu, H., Meng, Y. and Chen, T. (2023), "A Runge-Kutta scheme for smart control mechanism with computer-vision robotics", *Smart Struct. Syst., Int. J.*, **34**(2), 117-127. https://doi.org/10.12989/sss.2024.34.2.117

Chen, H., Huang, B., Zhang, H., Xue, K., Sun, M. and Wu, Z. (2024a), "An efficient Bayesian method with intrusive homotopy surrogate model for stochastic model updating", *Comput.-Aided Civil Infrastr. Eng.*, **39**(16), 2500-2516. https://doi.org/10.1111/mice.13206

Chen, R.S., Zhang, H.Y., Hao, X.K., Yu, H.X., Shi, T., Zhou, H.S., Wang, R.B., Zhao, Z.F. and Wang, P. (2024b), "Experimental study on ultimate bearing capacity of short thin-walled steel tubes reinforced with high-ductility concrete", *Structures*, **68**, 107109. https://doi.org/10.1016/j.istruc.2024.107109

Chen, Z.Y., Wang, R.Y., Meng, Y., Wu, H., Lai, B. and Chen, T. (2024c), "Enhancing mechanical performance of steel-tube-encased HSC composite walls: Experimental investigation and analytical modeling", *Steel Compos. Struct., Int. J.*, **52**(6), 647-656. https://doi.org/10.12989/scs.2024.52.6.647

Chen, Z.Y., Meng, Y., Wu, H., Gu, Z.Y. and Chen, T. (2024d), "Modified analytical AI evolution of composite structures with algorithmic optimization of performance thresholds", *Steel Compos. Struct., Int. J.*, **53**(1), 103-114. https://doi.org/10.12989/scs.2024.53.1.103

Chen, Z.Y., Wu, H., Wang, R.Y., Meng, Y. and Chen, T. (2024e), "Smart Lyapunov LMI criterion for TMD RC structure systems via deep reinforcement learning algorithms", *Smart Struct. Syst., Int. J.*, **34**(5), 283-297. https://doi.org/10.12989/sss.2024.34.5.283

Chen, Z.Y., Meng, Y., Wang, R.Y. and Chen, T. (2024f), "Intelligent optimal grey evolutionary algorithm for structural control and analysis", *Smart Struct. Syst., Int. J.*, **33**(5), 365-374. https://doi.org/10.12989/sss.2024.33.5.365

Chen, Z.Y., Meng, Y., Wu, H., Gu, Z.Y. and Chen, T. (2024g), "Applied AI neural network dynamic surface control to nonlinear coupling composite structures", *Steel Compos. Struct., Int. J.*, **52**(5), 571-581. https://doi.org/10.12989/scs.2024.52.5.571

Chen, Z.Y., Wang, R.Y., Meng, Y. and Chen, T. (2024h), "RC model control subjected to earthquakes using piecewise Lyapunov criterion in ambient intelligence", *Smart Struct. Syst., Int. J.*, **34**(3), 171-179. https://doi.org/10.12989/sss.2024.34.3.171

Chen, Z.Y., Meng, Y.H., Wang, R.Y. and Chen, T. (2025), "Reinforced concrete structural control subjected to design of fuzzy deep learning algorithm", *Adv. Concrete Constr., Int. J.*, **19**(1), 15-29. https://doi.org/10.10.12989/acc.2025.19.1.015

Ebadi, A., Auger, A. and Gauthier, Y. (2023), "Machine Learning Insights into Hypersonics Research Evolution: A 21st Century Perspective", *Arch. Adv. Eng. Sci.*, **2**(2), 79-92. https://doi.org/10.47852/bonviewAAES32021471

Fan, R., Pan, Y., Xiao, Y. and Wang, Z. (2024), "Investigation on flame propagation characteristics and critical ignition criteria of hydrogen jet", *Int. J. Hydrogen Energy*, **57**, 1437-1445. https://doi.org/10.1016/j.ijhydene.2024.01.126

Fukuda, Y., Feng, M.Q., Narita, Y., Kaneko, S.I. and Tanaka, T. (2013), "Vision-based displacement sensor for monitoring dynamic response using robust object search algorithm", *IEEE Sens. J.*, **13**, 4725-4732. https://doi.org/10.1109/JSEN.2013.2273309

Gong, B. and Li, H. (2024), "A couple Voronoi-RBSM modeling strategy for RC structures", *Struct. Eng. Mech., Int. J.*, **91**(3), 239-250. https://doi.org/10.12989/sem.2024.91.3.239

He, Y., Bao, M., Chen, Y., Ye, H., Fan, J. and Shi, G. (2024), "Accuracy characterization of Shack–Hartmann sensor with residual error removal in spherical wavefront calibration", *Light: Adv. Manuf.*, **4**(4), 393-403. https://doi.org/10.37188/lam.2023.036

Huang, H., Yao, Y., Zhang, W. and Zhou, L. (2023), "A push-out test on partially encased composite column with different positions of shear studs", *Eng. Struct.*, **289**, 116343. https://doi.org/10.1016/j.engstruct.2023.116343

Huang, H., Chen, Z., Zhao, M., Wang, B. and Ye, Y. (2024), "Seismic performance of frame with middle partially encased composite brace and steel-hollow core partially encased composite spliced frame beam", *J. Build. Eng.*, **95**, 110226. https://doi.org/10.1016/j.jobe.2024.110226

Huizinga, W., Poot, D.H., Guyader, J.M., Klaassen, R., Coolen, B.F., van Kranenburg, M., Van Geuns, R.J.M., Uitterdijk, A., Polfliet, M., Vandemeulebroucke, J. and Leemans, A. (2016), "PCA-based groupwise image registration for quantitative MRI", *Medical Image Anal.*, **29**, 65-78. https://doi.org/10.1016/j.media.2015.12.004

Koy, A. and Çolak, A.B. (2023), "The intraday high-frequency trading with different data ranges: A comparative study with artificial neural network and vector autoregressive models", *Arch. Adv. Eng. Sci.*, **2**(3), 123-133. https://doi.org/10.47852/bonviewAAES32021325

Lee, S., Kim, H. and Sim, S.H. (2022), "Nontarget-based displacement measurement using LiDAR and camera", *Automat. Constr.*, **142**, 104493. https://doi.org/10.1016/j.autcon.2022.104493

Li, H., Lu, H. and Li, Q. (2024), "Numerical investigations of the influences of valve spool structure on the eccentric jet flow

characteristic in high-pressure angle valves", *Energy*, **298**, 131378. https://doi.org/10.1016/j.energy.2024.131378

Li, G., Zhang, Y., Fan, S., Yu, F. and Wang, Y. (2025), "Dynamic-wave interference suppression based on angular increment assistance for underwater Imaging Polarization Sensor", *IEEE Transact. Instrum. Measur.*, **74**, 1-13. https://doi.org/10.1109/TIM.2024.3502730

Lienhart, W. (2017), "Geotechnical monitoring using total stations and laser scanners: critical aspects and solutions", *J. Civil Struct. Health Moni*t., **7**, 315-324. https://doi.org/10.1007/s13349-017-0228-5

Ling, H.I., Leshchinsky, D., Wang, J.P., Mohri, Y. and Rosen, A. (2009), "Seismic response of geocell retaining walls: experimental studies", *J. Geotech. Geoenv. Eng.*, **135**, 515-524. https://doi.org/10.1061/(ASCE)1090-0241(2009)135:4(515)

Liu, K., Jiao, S., Nie, G., Ma, H., Gao, B., Sun, C., Xin, D., Saha, T.K. and Wu, G. (2024), "On image transformation for partial discharge source identification in vehicle cable terminals of high-speed trains", *High Voltage*, **9**(5), 1090-1100. https://doi.org/10.1049/hve2.12487

Long, X., Iyela, P.M., Su, Y., Atlaw, M.M. and Kang, S.B. (2024a), "Numerical predictions of progressive collapse in reinforced concrete beam-column sub-assemblages: A focus on 3D multiscale modeling", *Eng. Struct.*, **315**, 118485. https://doi.org/10.1016/j.engstruct.2024.118485

Long, X., Li, H., Iyela, P.M. and Kang, S. (2024b), "Predicting the bond stress–slip behavior of steel reinforcement in concrete under static and dynamic loadings by finite element, deep learning and analytical methods", *Eng. Fail. Anal.*, **161**, 108312. https://doi.org/10.1016/j.engfailanal.2024.108312

Lu, D., Liang, J., Du, X., Ma, C. and Gao, Z. (2019a), "Fractional elastoplastic constitutive model for soils based on a novel 3D fractional plastic flow rule", *Comput. Geotech.*, **105**, 277-290. https://doi.org/10.1016/j.compgeo.2018.10.004

Lu, D., Zhou, X., Du, X. and Wang, G. (2019b), "A 3D fractional elastoplastic constitutive model for concrete material", *Int. J. Solids Struct.*, **165**, 160-175. https://doi.org/10.1016/j.ijsolstr.2019.02.004

Meng, S., Zhang, C., Shi, Q., Chen, Z., Hu, W. and Lu, F. (2023), "A robust infrared small target detection method jointing multiple information and noise prediction: Algorithm and benchmark", *IEEE Transact. Geosci. Remote Sens.*, **61**, 1-17. https://doi.org/10.1109/TGRS.2023.3295932

Meng, W., Xin, L., Jinshuai, S., Weiwei, L., Zhongzheng, F., Shuai, W., Jiaxu, K. and Wenguang, Y. (2024a), "A study on the reasonable width of narrow coal pillars in the section of hard primary roof hewing along the air excavation roadway", *Energy Sci. Eng.*, **12**(6), 2746-2765. https://doi.org/10.1002/ese3.1799

Meng, Y., Wu, H., Chen, Z.Y. and Chen, T. (2024b), "Experimental and AI based FEM simulations for composite material in tested specimens of steel tube", *Steel Compos. Struct., Int. J.*, **52**(4), 475-485. https://doi.org/10.12989/scs.2024.52.4.475

Meng, Y., Chen, Z.Y., Wang, R.Y. and Chen, T. (2024c), "Dynamic control of nonlinear structural systems by smart linear quadratic regulator algorithm", *Smart Struct. Syst., Int. J.*, **34**(4), 261-270. https://doi.org/10.12989/sss.2024.34.4.261

Pan, B., Qian, K., Xie, H. and Asundi, A. (2009), "Twodimensional digital image correlation for in-plane displacement and strain measurement: a review", *Meas. Sci. Technol.*, **20**, 062001. https://doi.org/10.1088/0957-0233/20/6/062001

Panah, A.K. and Yazdi, M. and Ghalandarzadeh, A. (2015), "Shaking table tests on soil retaining walls reinforced by polymeric strips", *Geotext. Geomembr.*, **43**, 148-161. https://doi.org/10.1016/j.geotexmem.2015.01.001

Perona, P. and Malik, J. (1990), "Scale-space and edge detection using anisotropic diffusion", *IEEE Transact. Pattern Anal. Mach. Intell.*, **12**(7), 629-639. 10.1109/34.56205

Rivaz, H., Karimaghaloo, Z. and Collins, D.L. (2014), "Selfsimilarity weighted mutual information: a new nonrigid image registration metric", *Med. Image Anal.*, **18**, 343-358. https://doi.org/10.1016/j.media.2013.12.003

Shi, M., Hu, W., Li, M., Zhang, J., Song, X. and Sun, W. (2023), "Ensemble regression based on polynomial regression-based decision tree and its application in the in-situ data of tunnel boring machine", *Mech. Syst. Signal Process.*, **188**, 110022. https://doi.org/10.1016/j.ymssp.2022.110022

Shinde, A.L. and Mandal, J.N. (2007), "Behavior of reinforced soil retaining wall with limited fill zone parameter", *Geotechn. Geol. Eng.*, **25**, 657-672. https://doi.org/10.1007/s10706-007-9138-3

Shu, J., Zhang, X., Li, W., Zeng, Z., Zhang, H. and Duan, Y. (2024), "Point cloud and machine learning-based automated recognition and measurement of corrugated pipes and rebars for large precast concrete beams", *Automat. Constr.*, **165**, 105493. https://doi.org/10.1016/j.autcon.2024.105493

Sun, Q., Wang, H., Liu, W., Zou, J., Ye, F. and Li, Y. (2024), "An Improved Stereo Visual-Inertial SLAM Algorithm Based on Point-and-Line Features for Subterranean Environments", *IEEE Transact. Vehicul. Technol.*, 1-16. https://doi.org/10.1109/TVT.2024.3492388

Sun, R., Wang, S., Li, M. and Zhu, Y. (2025), "An algorithm for large-span flexible bridge pose estimation and multi-keypoint vibration displacement measurement", *Measurement*, **240**, 115582. https://doi.org/10.1016/j.measurement.2024.115582

Taherdoost, H. and Mohebi, A. (2024), "Using SMART Method for Multi-criteria Decision Making: Applications, Advantages, and Limitations", *Arch. Adv. Eng. Sci.*, **2**(4), 1-10. https://doi.org/10.47852/bonviewAAES42022765

Tai, S., Bu, C., Wang, Y.L., Yue, T., Liu, H.L. and Wang, L.X. (2024), "Identification of aircraft longitudinal aerodynamic parameters using an online corrective test for wind tunnel virtual flight", *Chinese J. Aeronaut.*, **37**(9), 261-275. https://doi.org/10.1016/j.cja.2024.05.031

Tu, B., Ren, Q., Li, J., Cao, Z., Chen, Y. and Plaza, A. (2024), "NCGLF2: Network combining global and local features for fusion of multisource remote sensing data", *Inform. Fusion*, **104**, 102192. https://doi.org/10.1016/j.inffus.2023.102192

Vappou, J., Luo, J. and Konofagou, E.E. (2010), "Pulse wave imaging for noninvasive and quantitative measurement of arterial stiffness *In Vivo*", *Am. J. Hypertens.*, **23**(4), 393-398. https://doi.org/10.1038/ajh.2009.272

Wang, R.Y., Chen, Z.Y., Jiang, R. and Chen, T. (2022a), "NNDI decentralized evolved intelligent stabilization of large-scale systems", *Smart Struct. Syst., Int. J.*, **30**(1), 1-15. https://doi.org/10.12989/sss.2022.30.1.001

Wang, R.Y., Meng, Y., Chen, T. and Chen, Z.Y. (2022b), "Intelligent algorithm and optimum design of fuzzy theory for structural control", *Smart Struct. Syst., Int. J.*, **30**(5), 537-544. https://doi.org/10.12989/sss.2022.30.5.537

Wang, R.Y., Chen, Z.Y., Meng, Y. and Chen, T. (2023), "A novel smart criterion of grey-predictioncontrol for practical applications", *Smart Struct. Syst., Int. J.*, **31**(1), 69-78. https://doi.org/10.12989/sss.2023.31.1.069

Wang, J., Lin, S.Q., Tan, D.Y., Yin, J.H., Zhu, H.H. and Kuok, S.C. (2024a), "A Novel Method for Integrity Assessment of Soil-Nailing Works with Actively Heated Fiber-Optic Sensors", *J. Geotech. Geoenviron. Eng.*, **150**(8), 04024063. https://doi.org/10.1061/JGGEFK.GTENG-11790

Wang, K., Cao, J., Ye, J., Qiu, Z. and Wang, X. (2024b), "Discrete element analysis of geosynthetic-reinforced pile-supported embankments", *Constr. Build. Mater.*, **449**, 138448.

https://doi.org/10.1016/j.conbuildmat.2024.138448
Wang, M., Su, J., Qin, H., Shang, L., Kang, J., Liu, W., Li, M., Zhang, F., Li, X. and Fang, Z. (2024c), "Research on Active Advanced Support Technology of Backfilling and Mining Face", *Rock Mech. Rock Eng.*, **57**(9), 7623-7642. https://doi.org/10.1007/s00603-024-03808-7
Wang, S., Lin, S. and Yang, R. (2024d), "A lightweight convolutional neural network for multipoint displacement measurements on bridge structures", *Nonlinear Dyn.*, **112**(14), 11745-11763. https://doi.org/10.1007/s11071-024-09673-x
Wang, J., Bai, L., Fang, Z., Han, R., Wang, J. and Choi, J. (2024e), "Age of Information Based URLLC Transmission for UAVs on Pylon Turn", *IEEE Transact. Vehicular Technol.*, **73**(6), 8797-8809. https://doi.org/10.1109/TVT.2024.3358844
Wu, Y., Fan, Y., Zhou, S., Wang, X., Chen, Q. and Li, X. (2024), "Research on the cross-sectional geometric parameters and rigid skeleton length of reinforced concrete arch bridges: A case study of Yelanghu Bridge", *Structures*, **69**, 107423. https://doi.org/10.1016/j.istruc.2024.107423
Xiao, G., Xiao, Z., Zhou, P., Jia, X., Wang, N., Zhao, D. and Wei, H. (2024), "PPP based on factor graph optimization", *Measur. Sci. Technol.*, **35**(11), 116307. https://doi.org/10.1088/1361-6501/ad6680
Xu, B. and Guo, Y. (2022), "A novel DVL calibration method based on robust invariant extended Kalman filter", *IEEE Transact. Vehicular Technol.*, **71**(9), 9422-9434. https://doi.org/10.1109/TVT.2022.3182017
Xu, B., Wang, X., Zhang, J., Guo, Y. and Razzaqi, A.A. (2022), "A novel adaptive filtering for cooperative localization under compass failure and non-gaussian noise", *IEEE Transact. Vehicular Technol.*, **71**(4), 3737-3749. https://doi.org/10.1109/TVT.2022.3145095
Yao, Y., Huang, H., Zhang, W., Ye, Y., Xin, L. and Liu, Y. (2022), "Seismic performance of steel-PEC spliced frame beam", *J. Constr. Steel Res.*, **197**, 107456. https://doi.org/10.1016/j.jcsr.2022.107456
Yin, H., Zhang, G., Wu, Q., Cui, F., Yan, B., Yin, S., Soltanian, M.R., Thanh, H.V. and Dai, Z. (2024), "Unraveling overlying rock fracturing evolvement for mining water inflow channel prediction: A spatiotemporal analysis using ConvLSTM image reconstruction", *IEEE Transact. Geosci. Remote Sens.*, **62**, 1-17. https://doi.org/10.1109/TGRS.2024.3452937
Yoo, C. and Jung, H.S. (2004), "Measured behavior of a geosynthetic-reinforced segmental retaining wall in a tiered configuration", *Geotext. Geomembr.*, **22**, 359-376. https://doi.org/10.1016/S0266-1144(03)00064-5
Yu, S., Guan, D., Gu, Z., Guo, J., Liu, Z. and Liu, Y. (2024), "Radar Target Complex High-Resolution Range Profile Modulation by External Time Coding Metasurface", *IEEE Transact. Microw. Theory Techniq.*, **72**(10), 6083-6093. https://doi.org/10.1109/TMTT.2024.3385421
Zhang, C. (2023), "The active rotary inertia driver system for flutter vibration control of bridges and various promising applications", *Sci. China Technol. Sci.*, **66**(2), 390-405. https://doi.org/10.1007/s11431-022-2228-0
Zhang, S., Tan, D., Zhu, H., Pei, H. and Shi, B. (2024a), "Rheological behaviors of Na-montmorillonite considering particle interactions: A molecular dynamics study", *J. Rock Mech. Geotech. Eng.* https://doi.org/10.1016/j.jrmge.2024.07.003
Zhang, W., Lin, J., Huang, Y., Lin, B. and Liu, X. (2024b), "Experimental and numerical studies on flexural performance of composite beams under cyclic loading", *Structures*, **70**, 107728. https://doi.org/10.1016/j.istruc.2024.107728
Zhou, C. (2023), "Development Expectation Gap of Design-Build Contract Delivery in China's Civil Aviation Infrastructure Projects", *Arch. Adv. Eng. Sci.*, 1-11. https://doi.org/10.47852/bonviewAAES32021430
Zhou, X., Lu, D., Zhang, Y., Du, X. and Rabczuk, T. (2022), "An open-source unconstrained stress updating algorithm for the modified Cam-clay model", *Comput. Methods Appl. Mech. Eng.*, **390**, 114356. https://doi.org/10.1016/j.cma.2021.114356
Zi, J., Liu, T., Zhang, W., Pan, X., Ji, H. and Zhu, H. (2024), "Quantitatively characterizing sandy soil structure altered by MICP using multi-level thresholding segmentation algorithm", *J. Rock Mech. Geotech. Eng.*, **16**(10), 4285-4299. https://doi.org/10.1016/j.jrmge.2023.11.025